A crack propagation criterion based on Delta CTOD measured with 2D-digital image correlation technique

A. Ktari, M. Baccar, M. Shah, N. Haddar, H. F. Ayedi, Farhad Rezai-Aria

A crack propagation criterion based on ΔCTOD measured with 2D-digital image correlation technique

A. KTARI[1,2], **M. BACCAR**[1], **M. SHAH**[1], **N. HADDAR**[2], **H. F. AYEDI**[2] **and F. REZAI-ARIA**[1]

[1]*Université de Toulouse; INSA, UPS, Mines Albi, ISAE; ICA (Institut Clément Ader) Route de Tiellet, Campus Jarlard, Albi, France,* [2]*Laboratoire de Génie des Matériaux et Environnement (LGME), ENIS, Université de Sfax BP 1173-3038, Tunisia*

ABSTRACT The fatigue cracks growth rate of a forged HSLA steel (AISI 4130) was investigated using thin single edge notch tensile specimen to simulate the crack development on a diesel train crankshafts. The effect of load ratio, R, was investigated at room temperature. Fatigue fracture surfaces were examined by scanning electron microscopy. An approach based on the crack tip opening displacement range (ΔCTOD) was proposed as fatigue crack propagation criterion. ΔCTOD measurements were carried out using 2D-digital image correlation techniques. J-integral values were estimated using ΔCTOD. Under test conditions investigated, it was found that the use of ΔCTOD as a fatigue crack growth driving force parameter is relevant and could describe the crack propagation behaviour, under different load ratio R.

Keywords forged steel; crack propagation; digital image correlation; CTOD; J-integral.

NOMENCLATURE

a = Crack length
COD (or δ) = crack opening displacement
CTOD (or δ_t) = crack tip opening displacement
d_n = constant depending on materials properties
DIC = digital image correlation
E = young modulus
FCG = fatigue crack growth
FCGR = fatigue crack growth rate
J = J-integral
J_{max} = J-integral at maximal load
J_{min} = J-integral at minimum load
K = stress intensity factor
K_{op} = stress intensity factor at the crack opening load
K_{max} = stress intensity factor at maximal load
K_{min} = stress intensity factor at minimum load
n = strain hardening exponent
N = the number of cycles
R = fatigue load ratio
SENT = single edge notch specimen
SSY = small scale yielding
W = specimen width
α = material constant
$\delta_t^{\sigma_{max}}$ = crack tip opening displacement at maximal load
$\delta_t^{\sigma_{min}}$ = crack tip opening displacement at minimum load
ΔCOD (or $\Delta\delta$) = crack opening displacement range
ΔCTOD (or $\Delta\delta_t$) = crack tip opening displacement range
ΔJ = variation of the J-integral $= J_{max} - J_{min}$
$\Delta J^{\delta t}$ = variation of the J-integral calculated from experimental $\Delta\delta_t$

Correspondence: A. Ktari. E-mail: ahmedingmat@yahoo.fr

$\Delta K = K_{max} - K_{min}$ = stress intensity factor range
$\Delta K_{eff} = K_{max} - K_{op}$ = effective stress intensity factor range
ε_p = plastic strain
σ_0 = yield stress

INTRODUCTION

The crankshaft is an engine component that converts the linear piston movement into rotary motion while the force connecting rod is transformed to torque. It contains geometrical discontinuities or singularities, from which cracks can initiate and propagate until final fracture.[1–9] To predict the fatigue crack growth rate (FCGR) under different loading conditions, several models are proposed.[10–13] Nevertheless, the most simple and well known model to predict FCGR rate da/dN is a power law described by Paris and Erdogan[14] using stress intensity factor (SIF) range (K) as in Eq. (1):

$$\frac{da}{dN} = C(\Delta K)^m \tag{1}$$

where C and m are constants dependent on the materials and the environmental factors. This model can be quite useful in engineering applications. But it does address their physical phenomena that occur during crack propagation especially near the crack tip fields. Measuring changes in the compliance of cracked thin sheets 2024-T3 aluminium alloy, Elber, in 1971 has shown[15] the fatigue closure phenomenon at a remotely applied tensile stress. They attributed it to the formation of a residual compressive stress behind the crack tip. This implies that only the load range between the opening load P_{op} and the maximum load P_{max} can affect the damage of the crack tip during the load cycle. Hence, they proposed to modify Paris relationship using only the portion of the stress intensity range above the crack opening load, as presented in Eq. (2):

$$\frac{da}{dN} = C\left(\Delta K_{eff}\right)^m \tag{2}$$

where ΔK_{eff} is the effective SIF range. Most of the researchers consider the concept of crack closure as a crucial mechanism regarding its relationship with load ratio effects on the crack propagation in metallic materials.[16–21] To measure this crack closure, a number of techniques such as the electrical potential drop, the ultrasonic methods and the eddy current methods [22] were developed. Nevertheless, there are still significant difficulties to correlate the crack closure measurements with the crack growth behaviour in a consistent way.[23–26]

Several models exist in literature to predict the FCGR within structures. These models are based on the linear elastic fracture mechanics approach that assumes that crack propagates in the small scale yielding (SSY) conditions (i.e. the crack length is much larger than the crack tip plastic zone). Nevertheless, this assumption is not usually prevailed especially at high temperature or even at ambient temperature when the material presents a ductile behaviour (i.e. the crack propagates with considerable plastic deformation in the vicinity of the crack tip). Hence, the FCG should be studied under elastic plastic fracture mechanics approach. Indeed, an energy criterion based on the J-integral, defined by Rice,[27] is suggested. In order to achieve this, the crack tip opening displacement range (ΔCTOD) is considered as an FCGR criterion. The use of this parameter is interesting in the way that it allows to establish experimentally the cyclic J-integral values.[28,29] The ΔCTOD values are estimated from ΔCOD measurements, which are carried out using 2D-digital image correlation (DIC) methods.[30,31] The latter are non contact methods that can remove the errors introduced due to probing. Also because it is a ‘post test’ measurement system, the data can be analysed with different parameters. Multiple points of local measurements by ‘virtual strain gauges’ can be applied along the crack line. The data from these points are extrapolated up to the crack tip to obtain the CTOD values.[32,33] The full-field DIC displacement measurements have been the subject of many research over the past few decades. Dawicke and Sutton[34] have used the DIC method to measure the CTOA during the fracture tests of thin-sheet material (i.e. The CTOA is defined as the angle made by two straight lines: one line contained a point on the upper crack surface and the crack tip and the other line contained the crack tip and a point on the lower crack surface). Yusof and Withers[35] have used also the DIC to determine the crack tip position and stress intensity variations (K_I and K_{II}) for a pre-cracked aluminium CT specimen. Lopez-Crespo *et al.*[36] have applied a generalized approach to determine the SIFs K_I and K_{II} for any mixed mode (i.e. the complete range of mixed mode loading from pure mode I to pure mode II) measured directly from DIC displacement fields. This approach is presented using a centre fatigue cracked heat-treated 7010 T7651 aluminium plate. Roux and Hild[37] have also applied DIC to study the crack propagation in ceramic as a brittle material. Becker *et al.*[38] have presented a new methodology for evaluation of the J-integral domain based on DIC full-field displacement measurement. This methodology is tested and validated on three different specimen geometries for elastic, elastic–plastic and quasibrittle materials.

This paper aims to (i) study the fatigue crack behaviour of AISI 4130 forged steel used in train crankshafts under different load ratio, R, and (ii) apply ΔCTOD as crack propagation criterion micro scale 2D-DIC measurements.

EXPERIENCES

Material and specimen preparation

The experiments were carried out on single edge notched tensile (SENT) specimens machined from AISI 4130 forged steel and were taken from the counterweights of fractured train crankshaft. The chemical analysis of the crankshaft material was carried out using a spectroscopic metal analyzer (Jobin Yvon JY 48®), and the chemical composition is given in Table 1.

As mentioned earlier, fatigue experiments were carried out on SENT specimens (Fig. 1). All of these specimens were machined by a wire electrical discharge machining. Then, they were quenched from austenitizing temperature (900 °C) and subsequently tempered at 595 °C for 1 h to achieve a hardness of 235 HV_1 and a $R_{0.2}$ of 540 MPa at room temperature. The heat-treated steel (Fig. 2) presents a fine ferritic–perlitic microstructure, in which the grain size is in a range of 3–9 µm and some bainitic lathes. The heat-treated plates were electro-discharged and ground to form specimens' flat with a thickness of 1 mm. Then, the specimens were polished parallel to the loading axe down to 1 µm diamond pastes. Finally, these specimens were notched by a wire saw with a wire diameter of 0.3mm and pre-cracked under high-frequency cyclic loading until an initial crack length ranged from 0.8 to 1 mm.

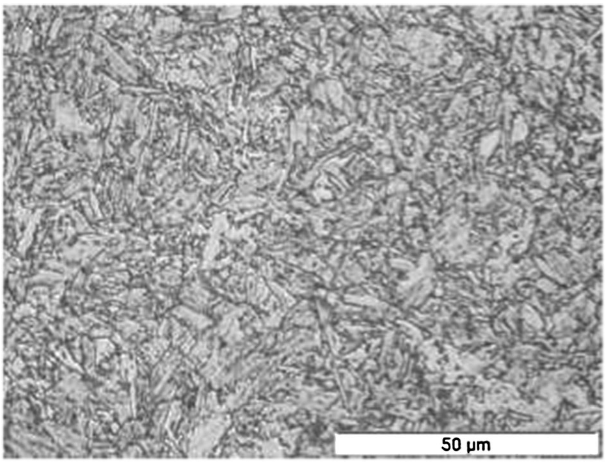

Fig. 2 Material microstructure (3% Nital etching) observed after heat treatment with optical microscope.

Fatigue crack growth tests

The fatigue crack propagation tests were carried out on a servo-hydraulic universal testing machine 'WALTER +BAI LFV 40'. Specimens were cycled under purely

Table 1 Chemical analysis of the crankshaft forged steel (AISI 4130)

Elements	C	Si	Mn	P	S	Cr	Mo	Ni
Weight %	0.263	0.236	0.55	0.01	0.006	1.02	0.176	0.196

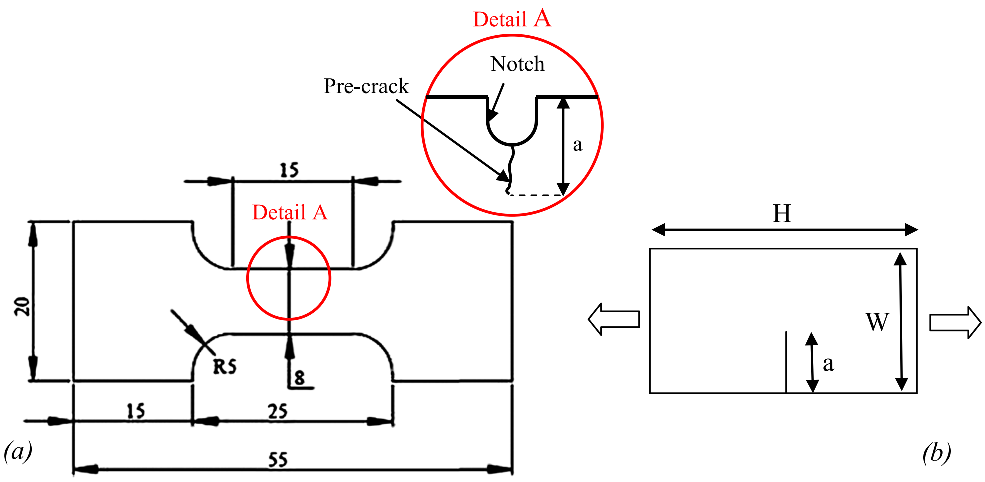

Fig. 1 Dimensions of SENT specimen (in mm). (a) Modified specimen and (b) normalized specimen.

tensile loading at room temperature using a sine waveform at a frequency of 10 Hz. In addition, two load ratios, $R(R = P_{min}/P_{max})$ of 0.1 and 0.7 were applied and held constant for each experiment, to study the effect of R on the FCGR. The maximum applied loads (P_{max}) ranged from 1.2 to 3.4 kN. This corresponds to a crack length and ΔK values ranges of 0.96–4.16 mm and 8–38 $\text{MPa}\sqrt{m}$, respectively. Under these loading conditions, the radius of the cyclic plastic zone around the crack tip is ranged from 0.047 to 0.495 mm ($R = 0.1$) and from 0.022 to 0.08 mm ($R = 0.7$) respectively in the beginning and end of each experiment. These values are calculated using Bathias and Pelloux model[39]as given:

$$r_{pc} = 0.1\left(\frac{\Delta K}{\sigma_0}\right)^2$$

The length of the crack was optically observed, *in situ* using a 'QUESTAR®' long distance travelling microscope, which was installed in front of the specimen as shown in Fig. 3.

Fracture surface examination

Fracture surfaces were prepared for examination using scanning electron microscopy (SEM) 'Nova nano SEM 450' operated at 20 keV. Several observations were made to characterize the fractography over the whole range of ΔK for each tested specimen.

ΔCTOD measurements

The crack length was observed at different prescribed lengths. A magnification of 1000 with a maximum optical resolution of 1.1 µm/pixel could be achieved. The field of view, depending on zoom, was between 0.375 and 8 mm. The microscope is connected to a CCD camera 'Sony EXWAVE HAD' with a resolution of 470 × 300 pixels to capture images throughout measurement cycles. The combination between the microscope and the camera provided 0.4 mm field of view and 400 horizontal lines on the CCD sensor. Theoretically, this configuration allows us to take an image resolution of 1 µm/pixel. Practically, the resolution does not exceed 1.54 µm/pixel. This might principally be due to the errors induced by machine vibrations.

The maximum number of pictures taken with a CCD camera is 25 per second. Indeed, it is impossible to have all details around the crack field under 10 Hz frequency. As a consequence, to record the video of crack while cycling, the frequency was decreased to 0.2 Hz, and loading signal was changed from sine to triangular (Fig. 4). Then, videos were downloaded and transformed into images using image analysis software iMovie HD®. Finally, the DIC was performed on images for each measurement using a commercially image correlation software 'VIC 2D® '.[40] The first measured image in any cycle was used as the reference image. Then, virtual gauges were placed at different distances behind the crack tip using two-subsets DIC displacement gauges (Fig. 5). Mostafavi and Marrow[41] have revealed that the size of the virtual gauges and their distance from the crack can noticeably change the COD values. Carrol *et al.*[30] have introduced and compared two full-field DIC method to a DIC based on displacement gauge method (i.e. each gauge consists of two subsets, one on each of the crack flanks) at relatively low, medium and high K experiments. They showed that crack opening levels calculated from the full-field effective K method is in agreement with displacement gauge closure levels far from the crack tip in the constant opening level region. Indeed, in this study, we supposed that subset size and their distance from the crack have no noticeable effect on the COD values. Subset size of 29 by 29 pixels square

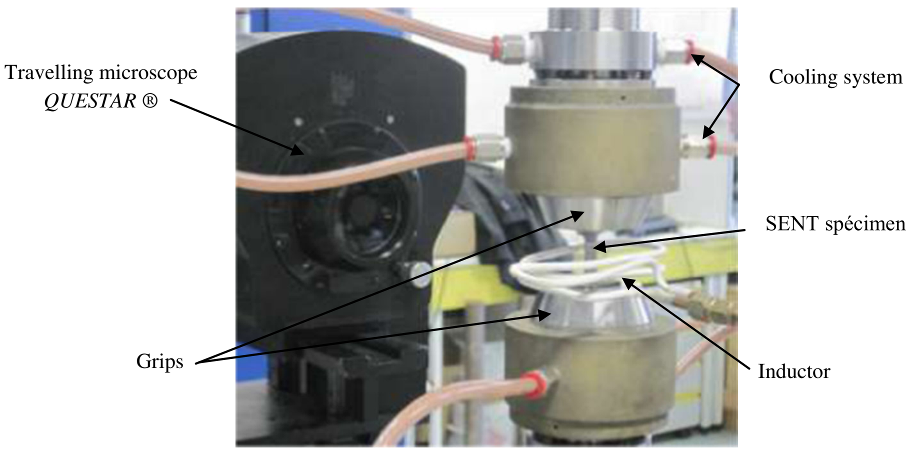

Fig. 3 General view of experimental setup.

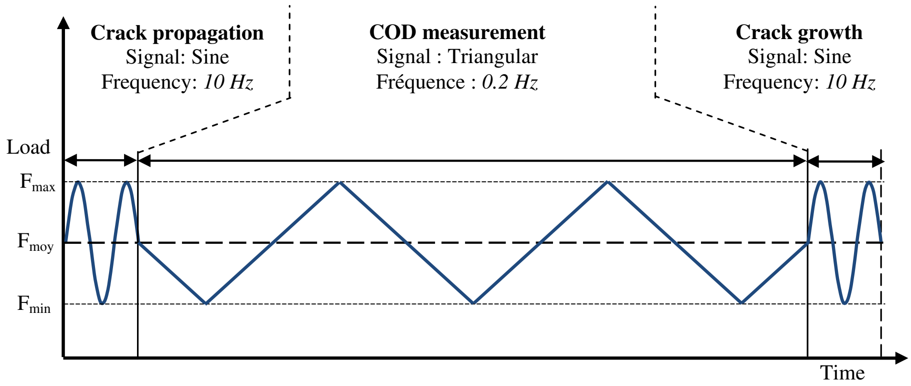

Fig. 4 A sequence of experimental COD measurement.

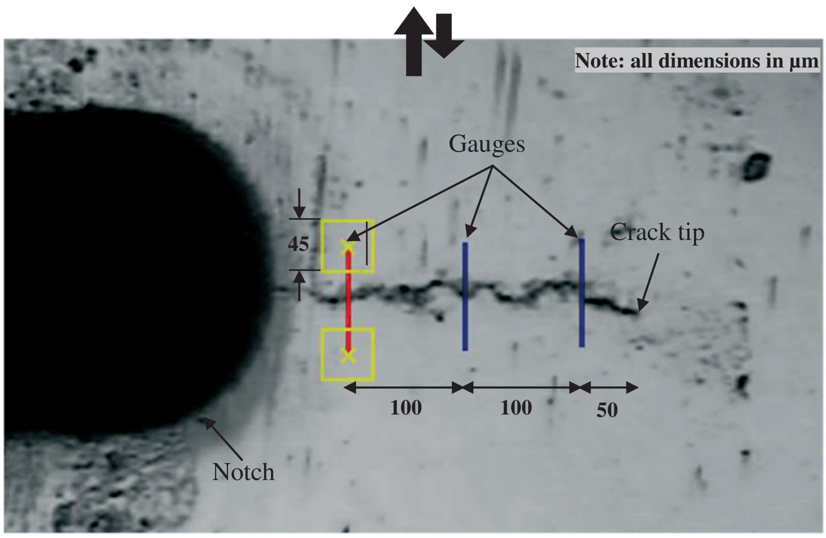

Fig. 5 Placement of virtual gauges behind crack tip in reference image (crack length = 800 µm, $R = 0.1$).

was used, corresponding to a gauge width of 45 µm and a typical length of 100 µm. Also, a step size of 5 was chosen[42] (i.e. the step size controls the spacing of the points that are analysed during correlation). The accuracy of the subset displacement was fixed at 0.1 pixels that corresponds to a precision of 0.154 µm. Figure 6 shows an example of measured ΔCOD ($\Delta\delta$) at six different crack length (a) during a cycle. These ΔCODs versus a was extrapolated to $a = 0$ to obtain ΔCTOD ($\Delta\delta_t$) that is considered as the opening of the crack tip for a given crack length.[43] The complete description of ΔCTOD calculation is described in Section 3.3.

RESULTS AND DISCUSSIONS

Effect of load ratio, *R*

The crack length evolutions versus number of cycle curves were plotted. Then the FCGR (da/dN) for each curve were presented as a function of the nominal ΔK or $\Delta\sqrt{J_I.E^*}$ in log–log scale to present Paris's law according to Eqs (3)–(5):

$$\Delta K_I = \Delta\sigma\sqrt{\pi a}.f\left(\frac{a}{W}\right) \tag{3}$$

$$f\left(\frac{a}{W}\right) = 1.0869 + 0.2383\left(\frac{a}{W}\right) + 1.9830\left(\frac{a}{W}\right)^2 - 2.8373\left(\frac{a}{W}\right)^3 + 2.5771\left(\frac{a}{W}\right)^4 \tag{4}$$

$$K_I = \sqrt{J_I.E^*} \Rightarrow \Delta K_I = \Delta\sqrt{J_I.E^*} \tag{5}$$

where 'a' is the crack length and 'W' is the specimen width. The expression of the correction factor (4) was developed and verified by Shah *et al.*[44] using finite element analysis for elastic and/or an elastoplastic behaviour at room temperature. E^* is apparent elastic modulus that is

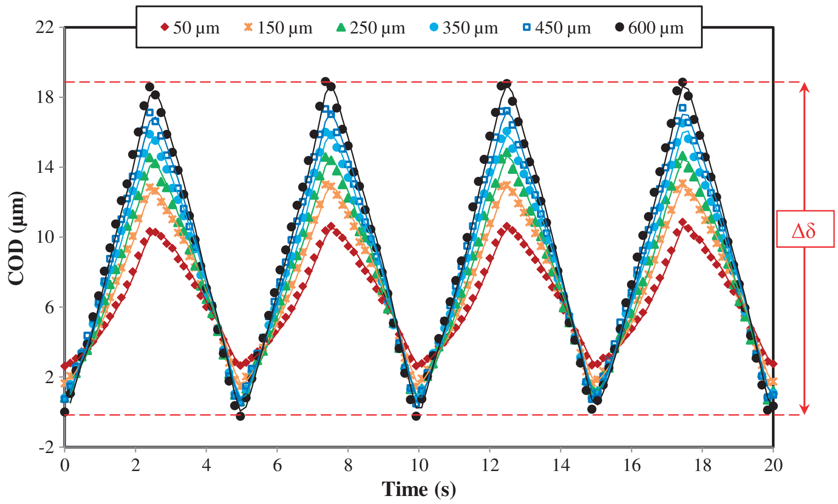

Fig. 6 Variation of COD as a function of a number of images during fatigue cycles on a specimen of 1 mm tested under a load ratio (crack length = 4560 µm, $R = 0.1$).

equal to E and $E/(1-\nu^2)$ for plane stress and plane strain conditions, respectively, and J is the energy release rate.

The effect of the load ratio on the conducted tests is shown in Fig. 7. The increasing of load ratio shows that threshold value decreases from 11 MPa$\sqrt{m}$ at $R = 0.1$ to 8 MPa$\sqrt{m}$ at $R = 0.7$. This result is in agreement with previous works conducted on ferrous and non ferrous metal.[45,46] The slope of the Paris law 'm' is constant and about 3.8. As expected, the increase of the R ratio increases da/dN for a given $\Delta\sqrt{J_I.E^*}$. It is obvious that the FCGR curve obtained at load ratio $R = 0.7$ is twice higher than that obtained at $R = 0.1$. This is usually explained by the presence of a crack closure effect at lower R ratio, which decreases the crack driving force.

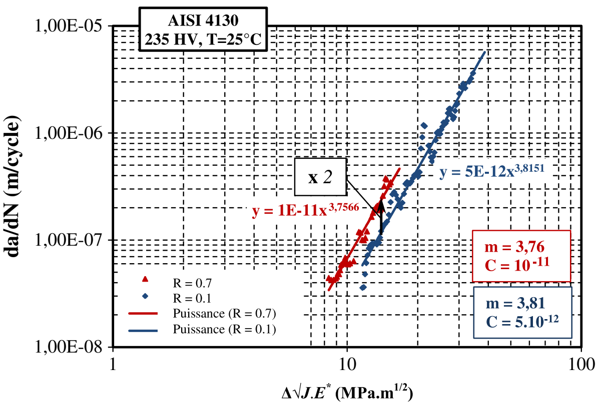

Fig. 7 Effect of load ratio R, on da/dN versus $\Delta\sqrt{J_I \cdot E^*}$ on FCRG of forged steel at room temperature (room temperature, $f = 10$ Hz).

Observation of fatigue fracture surfaces

The SEM fractographs of the tested specimens at load ratio $R = 0.1$ and 0.7 are investigated at different $\Delta\sqrt{J_I.E^*}$ values. For the first one, Fig. 8a shows that the fractured surface is flat for relatively low (11–16 MPa $\sqrt{m}$) and medium values (16–30 MPa $\sqrt{m}$) of $\Delta\sqrt{J_I.E^*}$ and presents several beach marks characteristics of the progressive propagation of the crack front during an experiment. In general, the presence of beach marks on fatigue fracture surface reveals a change in crack growth conditions. However, their presence in this case can be attributed to the frequency changes during the experiment (i.e. when we pass from sine to triangular signal to take video). The SEM observations of the crack front are linear and perpendicular on loading direction. This proves that this specimen is probably tested under plane strain condition at low and medium $\Delta\sqrt{J_I.E^*}$ values, which corresponds approximately to a crack length less than 3.6 mm. Additional observations carried out at the specimen crack profile with optical microscope show branching and decohesion of grain boundaries (Fig. 8d), which proves that crack propagation is mostly intergranular in this stage.

For long crack length (i.e. near $\Delta K_{I max} = \Delta\sqrt{J_I.E^*}_{max}$), the fractured surface presents several ratchet marks indicating the boundary between adjacent crack planes (Fig. 8b). Also, Fig. 8b shows the presence of river marks that is frequently a characteristic of a relatively fast-growing fatigue crack zone as well as an increase in shearing plane formations due to the large plastic zone size. Relying on the aforementioned information, it is clear that the condition of the crack propagation was changed from SSY to large

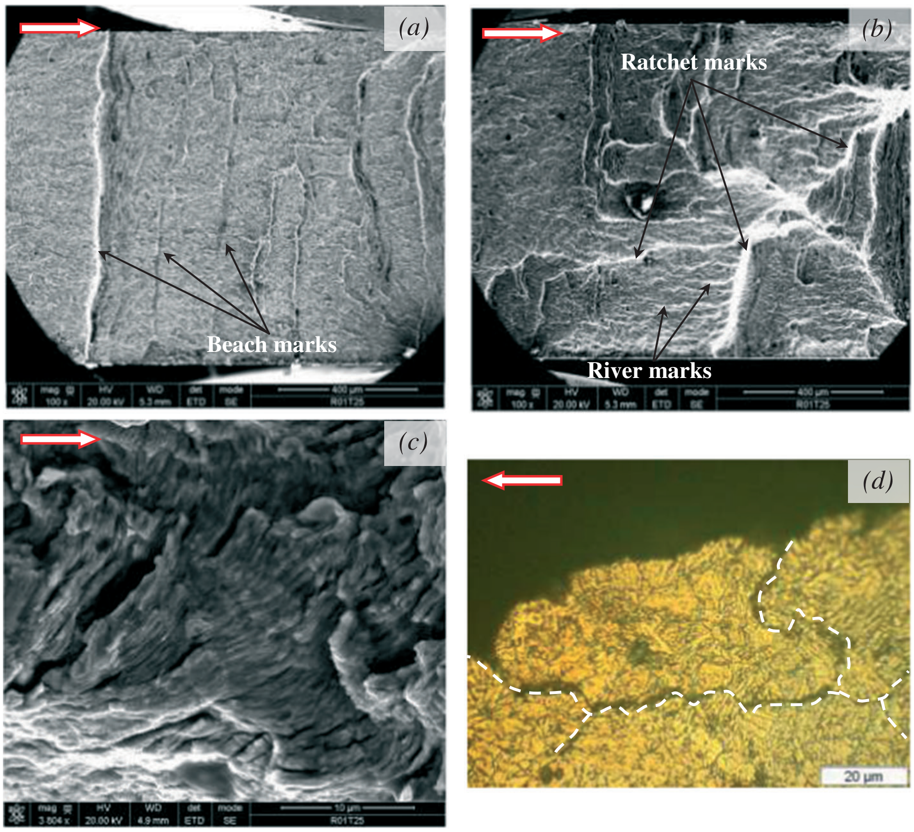

Fig. 8 Fatigue fractured surface of tested specimen $R = 0.1$ observed with SEM. (a) Low and medium $\Delta\sqrt{J_I \cdot E^*}$ values, (b) high $\Delta\sqrt{J_I \cdot E^*}$ values, (c) fatigue striation and micro-cracks (shear planes) and (d) crack branching and grain boundary decohesion.

scale yielding for approximately high $\Delta\sqrt{J_I.E^*}$ values ranging from 30 to 38 MPa $\sqrt{m}$, which corresponds to the fatigue fracture toughness value.

It is to be noted that fatigue striations were observed in all propagation stages (i.e. all $\Delta\sqrt{J_I.E^*}$ range values), which proves the ductile behaviour of the material. Figure 8c shows fatigue striations near the end of the crack propagation where each striation measures approximately 0.92 µm corresponding to a local FCGR of 9.2×10^{-7} m/cycle ($\Delta\sqrt{J_I.E^*} \simeq 25$–30 MPa$\sqrt{m}$).

For the second one (i.e. the fatigue fracture surface of the tested specimen at $R = 0.7$), Fig. 9a shows that the fatigue fracture surface was also flat in the beginning of crack propagation (i.e. low $\Delta\sqrt{J_I.E^*}$ values) with transgranular fracture mode. This fracture mechanism can be explained, in this stage, by the fact that the grain size, and the cyclic plastic zone size are in the same order.

The increase of the crack length and subsequently the value of $\Delta\sqrt{J_I.E^*}$ changes the propagation mode to mixed intergranular and transgranular with the presence of some beach marks (Fig. 9b). The fatigue fracture surface shows also that the crack front is linear and perpendicular on loading direction in all stages of the fatigue crack propagation. This proves that the specimen is probably tested under plane strain condition. Figure 9c shows intense localized deformation in slip bands near the crack tip that leads to the creation of new crack surfaces by shear decohesion and to create the 'zig-zag' crack path. This mechanism is dominant when cyclic plastic zone size is sufficiently large compared to the grain dimension.[47,48]

Application of CTOD as a fatigue crack propagation criterion

The *J*-integral approach presumes deformation plasticity and treats elastic–plastic materials as a nonlinear elastic material. This cause problems when using the cyclic *J*-integral (ΔJ) approach proposed by Dowling,[29] because the material unloads has to follow the same path as the loading curve. However, this is not the case because common materials show an elastoplastic behaviour, which while unloading simply follows a linear elastic path. Chow[49] has performed a detailed critical analysis of ΔJ parameters. Despite this critical analysis, ΔJ has been successfully applied to elastic–plastic fatigue crack growth.[50–53]

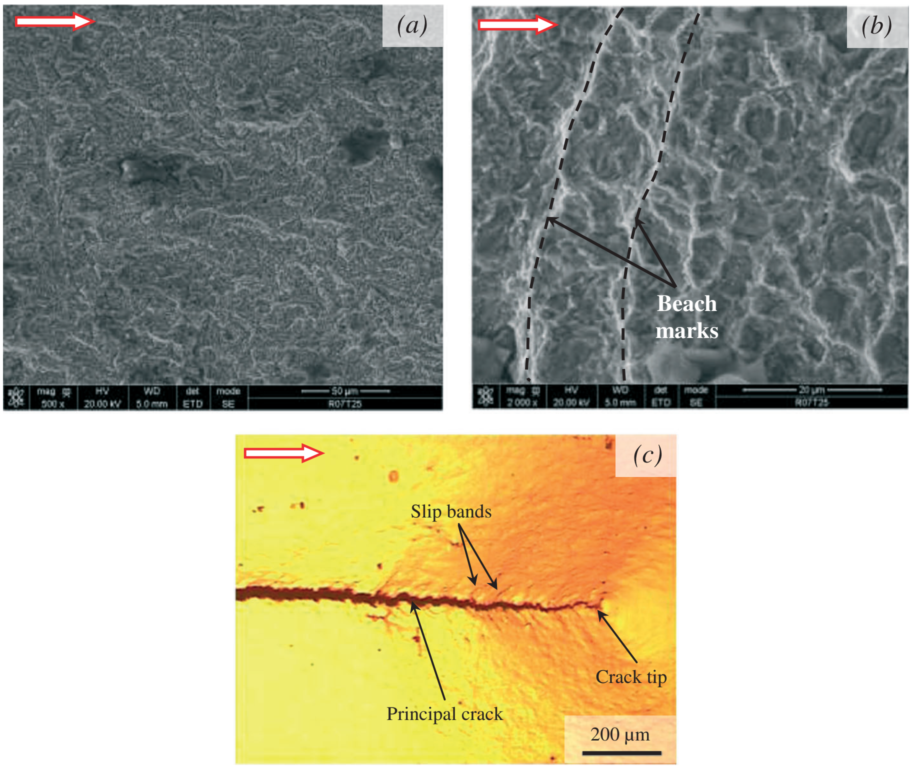

Fig. 9 Fatigue fracture surface of tested specimen at $R = 0.7$. (a) Near threshold fatigue crack growth, (b) high $\Delta\sqrt{J_I \cdot E^*}$ values and (c) profile of crack propagation at crack length, Clength = 2380 µm (medium $\Delta\sqrt{J_I \cdot E^*}$ values range).

The relationship between J and CTOD is proposed by Rice[27] and extensively reviewed by Shih[28] among others, principally Hutchinson, Tracey, McMeeking and McClintock.[54–57] The calculations are based on monotonic loading of the crack tip. The monotonic plastic strain is related to the stress in power law hardening material relationship given in Eq. (6):

$$\varepsilon_p = \alpha\left(\frac{\sigma}{\sigma_0}\right)^{n-1}\frac{\sigma}{E} \tag{6}$$

where E, α, n and σ_0 represent Young's modulus, a material constant, the hardening exponent and the yield stress of the material, respectively.

Based on the power low description, Hutchinson,[54] Rice and Rosengren[58] (HRR) showed that the stress and strain field in the vicinity of the crack are

$$\sigma_{ij} = \sigma_0\left(\frac{JE}{\alpha\sigma_0^2 I_n r}\right)^{1/(n+1)}\sigma_{ij}(\theta, n) \tag{7}$$

$$\varepsilon_{ij} = \frac{\alpha\sigma_0}{E}\left(\frac{JE}{\alpha\sigma_0^2 I_n r}\right)^{n/(n+1)}\varepsilon_{ij}(\theta, n) \tag{8}$$

where r, θ are polar coordinates centred at crack tip, I_n is an integration constant and $\sigma_{ij}(\theta,n)$ and $\varepsilon_{ij}(\theta,n)$ are dimensionless functions of the hardening exponent n. Equations (7) and (8) are valid for both plane stress or plane strain conditions. The J-integral represents the amplitude of HRR singularity described by Eq. (9). The crack opening profile δ_t may be presented in a similar form (Fig. 10a). Thus, the edge of the crack ($\theta = \pm\pi$) are given by

$$\begin{aligned}\frac{\delta}{2} &= \frac{\alpha\sigma_0}{E}\left(\frac{JE}{\alpha\sigma_0^2 I_n}\right)^{n/(n+1)} r^{1/(n+1)} u_y(n)\\ u_x &= \frac{\alpha\sigma_0}{E}\left(\frac{JE}{\alpha\sigma_0^2 I_n}\right)^{n/(n+1)} r^{1/(n+1)} u_x(n)\end{aligned} \tag{9}$$

where u_x and u_y are displacement in the x and y directions respectively, while $\delta = 2u_y$. The definition of δ_t suggested by Rice[27] and reviewed by Tracey[53] (Fig. 10b) defines δ_t as the opening distance between the intercept of two 45° lines drawn back from the crack tip with the deformed profile. At the intercept,

$$r - u_x = \frac{\delta}{2} \tag{10}$$

Under linear elastic conditions, the value of δ that satisfies Eqs (9) and (10) is given by Shih[28] (Eq. (11)):

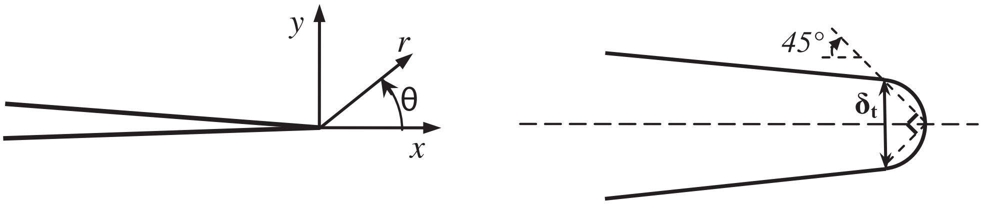

(a) Sharp crack *(b) Deformed profile*

Fig. 10 Sharp and deformed crack showing the 45° procedure for defining δ_t.

$$\delta_t = d_n \frac{J}{\sigma_0} \tag{11}$$

This expression is valid for both plane stress and plane strain condition. The coefficient d_n is a function of the material properties. It varies slightly with σ_0/E but significantly with n. For elastic-perfectly plastic materials and under plain strain condition, the value of d_n approaches 0.78 when $n \to \infty$. The complete evolution of d_n with respect to n and σ_0/E is shown in Fig. 11.

The model presented earlier is basically used for the monotonic loading of the cracked specimen. However, in this study, the model should be adapted in such a way to be coherent with the cyclic loading of the cracked SENT specimen. Indeed, some assumptions that have been made regarding to the state of stress and strain in SENT specimens are (i) specimen is loading under plane strain condition according to SEM fractured surfaces observation and (ii) all used material properties are obtained from cyclic tests (i.e. LCF total strain ($R_\varepsilon = -1$)); control tests are conducted on a 250 kN servo-hydraulic machine 'Schenck Hydropuls PSB®' at room temperature for variable total strain range ($\varepsilon = \pm 0.3$–1%). Shih's model[28] has been modified in such a way that we can calculate the crack driven force from $\Delta\delta_t$ as presented in Eq. (12):[49]

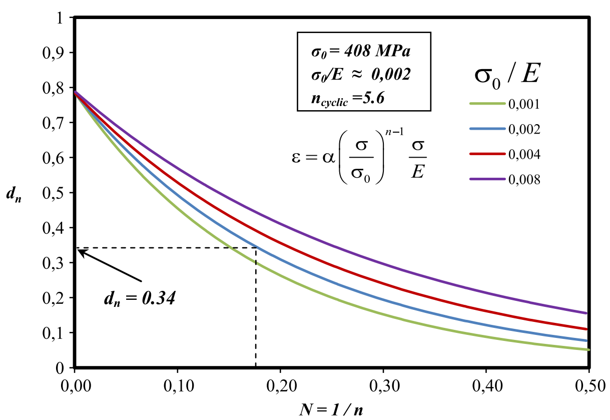

Fig. 11 Variation of d_n with and σ_0/E for plane strain condition.[28]

$$\Delta\delta_t = d_n \frac{\Delta J_I}{\sigma_0} \text{ with } \Delta\delta_t = \delta_t^{\sigma_{max}} - \delta_t^{\sigma_{min}} \tag{12}$$

Eq.(5)$\left(K_I{}^2 = J_I.E^*\right)$ and

$$\text{Eq.}(12) \Rightarrow \begin{cases} \delta_t^{\sigma_{\max}} = d_n \dfrac{J_{I\max}}{\sigma_0} = d_n \left(\dfrac{K_{I\max}^2}{E^* \sigma_0}\right) \\ \delta_t^{\sigma_{\min}} = d_n \dfrac{J_{I\min}}{\sigma_0} = d_n \left(\dfrac{K_{I\min}^2}{E^* \sigma_0}\right) \end{cases} \tag{13}$$

$$\text{Eq.}(13) \Rightarrow \Delta\delta_t = d_n \left(\frac{K_{I\max}^2}{E^* \sigma_0}\right) - d_n \left(\frac{K_{I\min}^2}{E^* \sigma_0}\right) \tag{14}$$

Equation (14) shows that ΔK_I depends on the square root of the $\Delta\delta_t$. The load ratio is also taken into account to present a coherent fatigue crack propagation law:

$$R = \frac{K_{I\min}}{K_{I\max}} \tag{15}$$

All mathematical treatment from Eqs (16) to (21) are formulated by Shah[59]

$$\text{Eqs (14) and (15)} \Rightarrow \Delta\delta_t = d_n \left(\frac{K_{I\max}^2}{E^* \sigma_0}\right) - \frac{d_n}{E^* \sigma_0} \left(R \cdot K_{I\max}\right)^2 \tag{16}$$

$$\Rightarrow \Delta\delta_t = \frac{d_n}{E^* \sigma_0} K_{I\max}^2 \left(1 - R^2\right) \tag{17}$$

Equation (17) may be used to calculate the SIF range from ΔCTOD denoted $\Delta K_{I\max}^{\delta t}$:

$$K_{I\max}^{\delta t} = \sqrt{\frac{E^* \sigma_0 \Delta\delta_t}{d_n \left(1 - R^2\right)}} \tag{18}$$

$$\Delta K_I^{\delta t} = K_{I\max}^{\delta t} - K_{I\min}^{\delta t} = \left(1 - R_{app}\right) \sqrt{\frac{E^* \sigma_0 \Delta\delta_t}{d_n \left(1 - R^2\right)}} \tag{19}$$

where R is used to calculate $K_{I\max}^{\delta t}$ parameter and R_{app} is any value of the applied load ratio. In the case where the plasticity at the crack tip cannot be ignored, we replace K_{Imax}^2/E^* by J_{Imax}:

$$J_{Imax}^{\delta t} = \frac{\sigma_0 \Delta\delta_t}{d_n\left(1 - R^2\right)} \tag{20}$$

$$\Delta J_I^{\delta t} = \left(1 - R_{app}^2\right) \frac{\sigma_0 \Delta\delta_t}{d_n\left(1 - R^2\right)} \tag{21}$$

The $\Delta J^{\delta t}$ is calculated from optical measurements of ΔCTOD (or $\Delta\delta_t$). Taking the crack tip as the origin, a number of virtual extensometers at specified distances are placed in the order behind the crack tip. Each extensometer gives a Δδ (or ΔCOD) values. Obviously the extensometer that is further away will show higher ΔCOD values (Fig. 6). Thus all the Δδ values are plotted against the position of the extensometer and extrapolated to the crack tip as shown in Figs 12 and 13. The evolution of $\Delta\delta_t$ versus the crack length is presented in Fig. 14. It

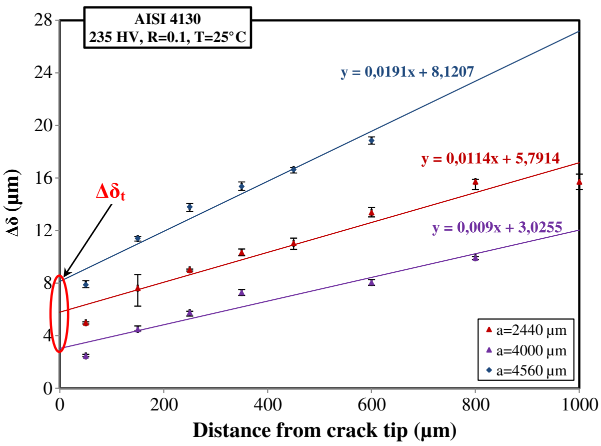

Fig. 12 Evolution of $\Delta\delta$ as a function of extensometer position behind the crack tip ($R = 0.1$).

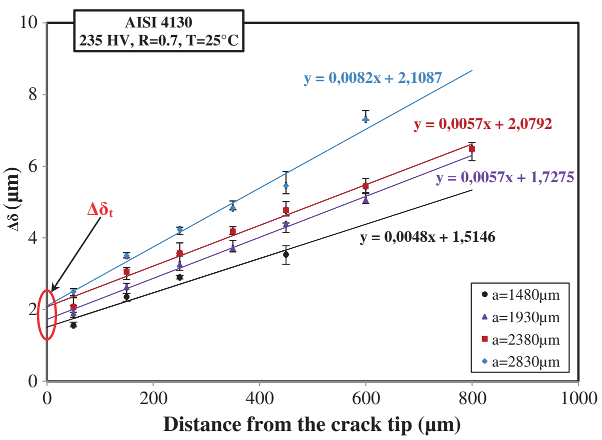

Fig. 13 Evolution of $\Delta\delta$ as a function of extensometer position behind the crack tip ($R = 0.7$)

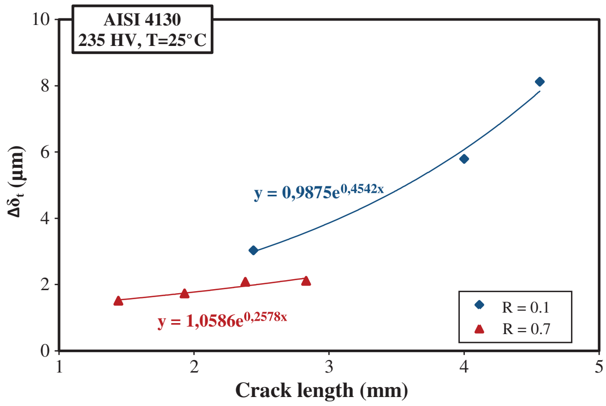

Fig. 14 ΔCTOD variation law as a function of crack length ($R = 0.1$ and 0.7) (room temperature, $f = 10$ Hz).

appears that the difference between these curves is relatively small at short crack length and increases continuously with the crack length. The FCGR criterion based on *J*-integral is defined as:

$$\frac{da}{dN} = A\left(\sqrt{\Delta \mathcal{J}_I^{\delta t} E^*}\right)^m \tag{22}$$

The evolution of $\sqrt{\Delta J_I^{\delta t} E^*}$ measured by using $\Delta\delta_t$ at room temperature and for two conditions of crack propagation of $R = 0.1$ and 0.7 are compared in the Fig. 15. The values of the $\sqrt{\Delta J_I^{\delta t} E^*}$ are higher for the specimen tested at $R = 0.1$. The FCGR curves based on this criterion are plotted in Fig. 16. It is clear that curves are superposed and can generate a master FCGR curve in which crack closure phenomena is ignored in a greater part. The advantage of this approach, based on the calculation of ΔCTOD with optical techniques, is that $\Delta J_I^{\delta t}$ is a macroscopic parameter that does not need any other detailed quantitative microscopic models to describe FCGR.

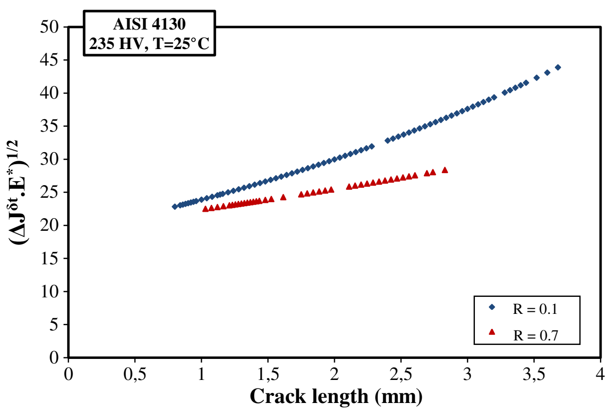

Fig. 15 Evolution of $\sqrt{\Delta J^{\delta^t} \cdot E^*}$ versus Crack length for different stress ratio ($R = 0.1$ and 0.7) (room temperature, $f = 10$ Hz).

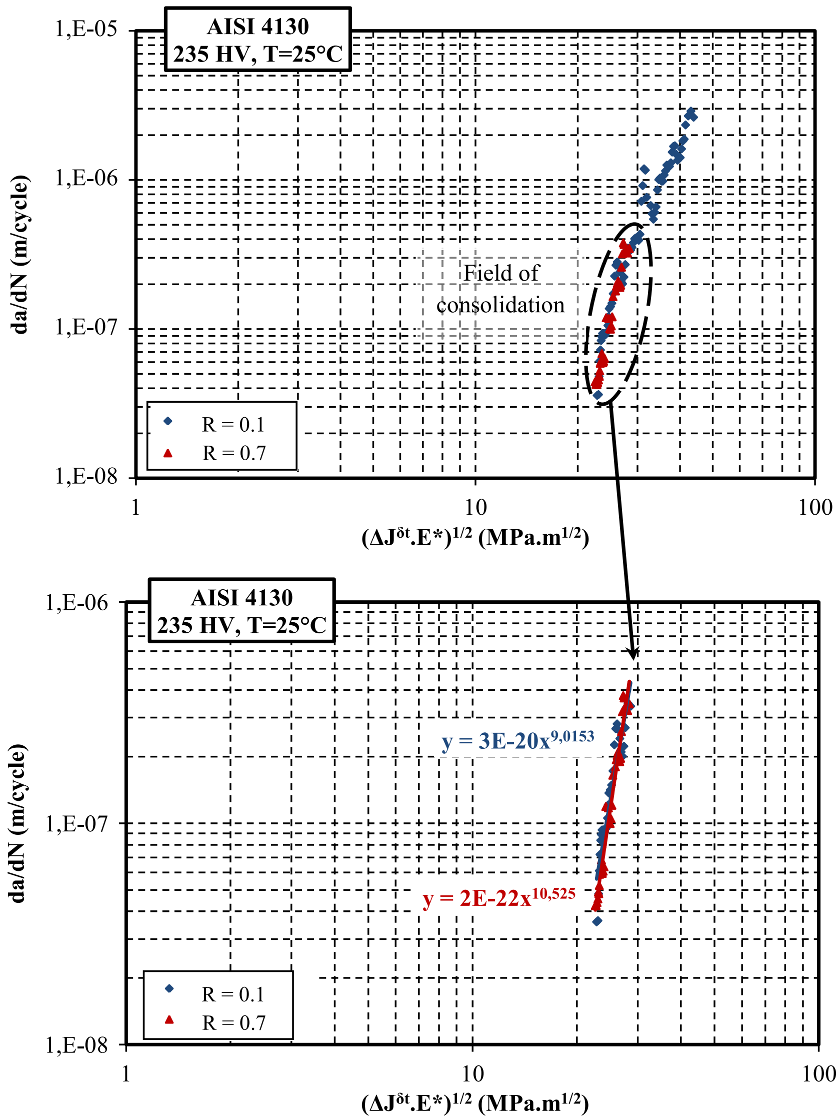

Fig. 16 Evolution of $\sqrt{\Delta J^{\delta t} \cdot E^{*}}$ as a FCRG parameter at $R = 0.1$ and 0.7 (room temperature, $f = 10$ Hz).

CONCLUSION

The FCG behaviour of AISI 4130 forged steel used in train crankshaft applications was studied for two different load ratio ($R = 0.1$ and 0.7) at room temperature. It was found that FCGR at load ratio, $R = 0.7$ was twice higher than that obtained at $R = 0.1$. The increase of FCGR was mostly explained by the presence of the crack closure phenomenon at $R = 0.1$, which can decrease the crack tip driven force.

The cyclic *J*-Integral as fatigue crack propagation criterion was used. It was determined from the experimental ΔCTOD ($\Delta\delta_t$) measured using direct optical observation of the fatigue crack propagation. It was found that the use of ΔCTOD as a crack driving force parameter, under tested parameter is interesting and presents an R independent alternative to the simulated ΔK parameter. This method, which is based on an optical measurement, can be a very interesting technique to predict the structures lifetime especially when SSY condition is not respected (i.e. when plasticity around the crack tip becomes important). However, it will be interesting to check the validity of this presented methodology for other experimental conditions, especially at high temperature.

REFERENCES

1 Ktari, A., Haddar, N. and Ayedi, H. F. (2011) Fatigue fracture expertise of train engine crankshafts. *Engineering Failure Analysis*, **18**, 1085–1093.

2 Espadafor, F. J., Villanueva, J. B. and Garcia, M. T. (2009) Analysis of a diesel generator crankshaft failure. *Engineering Failure Analysis*, **16**, 2333–2341.
3 Fonte, M. and de Freitas, M. (2009) Marine main engine crankshaft failure analysis: a case study. *Engineering Failure Analysis.*, **16**, 1940–1947.
4 Bayrakçeken, H., Tasgetiren, S. and Aksoy, F. (2007) Failure of a single cylinder engines crank shafts. *Eng Fail Anal*, **14**, 725–30.
5 Asi, O. (2006) Failure analysis of a crankshaft made from ductile cast iron. *Engineering Failure Analysis*, **13**, 1260–1267.
6 Wang, C., Zhao, C. and Wang, D. (2004) Analysis of an unusual crankshaft failure. *Engineering Failure Analysis*, **12**, 465–473.
7 Pandey, R. K. (2003) Failure of diesel-engine crankshaft. *Engineering Failure Analysis*, **10**, 165–175.
8 Silva, F. S. (2003) Analysis of vehicle crankshaft failure. *Engineering Failure Analysis*, **10**, 605–616.
9 Bhaumik, S. K., Rangaragu, R., Venkataswamy, M. A., Bhaskaran, T. A. and Parameswara, M. A. (2001) Fatigue fracture of crankshaft of an aircraft engine. *Engineering Failure Analysis*, **9**, 255–263.
10 Walker, E. K. (1970) The effect of stress ratio during crack propagation and fatigue for 2024-T3 and 7076-T6 aluminum. In: Effect of environment and complex load history on fatigue life, ASTM STP 462. American Society for Testing and Materials, Philadelphia, 1–14.
11 Forman, R. G. (1972) Study of fatigue crack initiation from flaws using fracture mechanics theory. *Engineering Fracture Mechanics*, **4**(2), 333–345.
12 Collipriest, J. E. (1972) An experimentalist's view of the surface flaw problem. The Surface Crack: Physical Problems and Computational Solutions. American Society of Mechanical Engineers, New York, 43–62.
13 McEvily, A. J. (1974) Phenomenological and microstructural aspects of fatigue. Presented at the Third International Conference on the Strength of Metals and Alloys, Cambridge, England, published by The Institute and The Iron and Steel Institutes, Publication, W36, 204–213.
14 Paris, P. C. and Erdogan, F. (1960) A critical analysis of crack propagation laws. *Journal of Basic Engineering*, **85**, 528–534.
15 Elber, W. (1971) The significance of fatigue crack closure. ASTM STP 415, 230–242.
16 Antunesa, F. V., Rodriguesa, D. M. and Brancob, R. (2010) An analytical model of plasticity induced crack closure. *Procedia Engineering*, **2**, 1005–1014.
17 de Matos, P. F. P. and Nowell, D. (2008) Numerical simulation of plasticity induced fatigue crack closure with emphasis on the crack growth scheme: *2D and 3D analyses*. *Engineering Fracture Mechanics*, (75), 2087–2114.
18 Andersson, M., Persson, C. and Melin, S. (2006) Experimental and numerical investigation of crack closure measurements with electrical potential drop technique. *International Journal of Fatigue*, **28**, 1059–1068.
19 David, T. (1992) The definition and measurement of crack closure. *Engineering Fracture Mechanics*, **43**, 109–115.
20 Shaw, D. and May, I. (1979) Crack closure during fatigue crack propagation, ASTM STP34916S, 233–241.
21 Clark, C. K. and Cassatt, G. C. (1977) A study of fatigue crack closure using electric potential and compliance techniques. *Engineering Fracture Mechanics*, **9**, 671–688.
22 Schijve, J. Fatigue crack closure: observation and technical significance, ASTM – STP 982; 5–34.
23 Josefson, B. L., Svensson, T., Ringgsberg, J. W., Gustafsson, T. and De Mare, J. (2000) Fatigue life and crack closure in specimens subjected to variable amplitude loads under plain strain conditions. *Engineering fracture mechanics*, **66**, 587–600.
24 James, M. N. (1997) Some unresolved issues with fatigue crack closure measurement, mechanism and interpretation problems, advances in fracture research. Proceedings of the Ninth International Conference on Fracture, Sydney, (eds. B. L. Karihaloo *et al*), Australia, April 1997, Pergamon Press, **5**, 2403–2414, ISBN 008 042820 7.
25 Macha, D. E., Corby, D. M., Jones, J. W. (1979) On the variation of fatigue crack-opening load with measurement location, *Proc Soc Exp Stress Analysis* **36**, 207–213.
26 Shin, C. S., Smith, R. A. (1985) Fatigue crack growth from sharp notches. *International Journal of Fatigue* **7**, 87–93.
27 Rice, J. R. (1968) A path independent integral and the approximate analysis of strain concentration by notches and cracks. *Journal of applied mechanics*, **35**, 379–386.
28 Shih, C. F. (1981) Relationship between the J-integral and the crack opening displacement for stationary and extending cracks. *J. Mech. Phys. Solids*, **29**, 305–326.
29 Dowling, N. E. and Begley, J. A. (1976) Fatigue Crack Growth During Gross Plasticity and the J-integral in Mechanics of Crack Growth, STP 590, ASTM, Philadelphia, 82–102.
30 Carroll, J., Efstathiou, C., Lambros, J., Sehitoglu, H., Hauber, B., Spottswood, S. and Chona, R. (2009) Investigation of fatigue crack closure using multiscale image correlation experiments. *Engineering Fracture Mechanics*, **76**, 2384–2398.
31 Nowell, D., Kartal, M. E. and DE Matos P. F. P. (2013) Digital image correlation measurement of near-tip fatigue crack displacement fields: constant amplitude loading and load history effects. *Fatigue Fract Engng Mater Struct*, **36**, 3–13.
32 Carrol, J. D., Abuzaid, W., Lambros, J. and Sehitoglu, H. (2013) High resolution digital image correlation measurements of strain accumulation in fatigue crack growth. *International Journal of Fatigue*, **57**, 140–150.
33 Sutton, M. A., Zhao, W., McNeill, S. R., Helm, J. D., Piascik, R. S. and Riddell, W. T. (1999) Local crack closure measurement: development of a measurement system using computer vision and a far-field microscope, ASTM - STP, 145–156.
34 Dawicke, D. S. and Sutton, M. A. (1994) CTOA and crack-tunneling measurements in thin sheet 2024-T3 aluminum alloy. *Exp. Mech.*, **34**(4), 357–368
35 Yusof, F. and Withers, P. J. (2009) Real-time acquisition of fatigue crack images for monitoring crack-tip stress intensity variations within fatigue cycles. *J. Strain Anal. Eng. Des.*, **44**(2), 149–158.
36 López-Crespo, P., Shterenlikht, A., Patterson, E. A., Withers, P. J. and Yates, J. R. (2008) The stress intensity of mixed mode cracks determined by digital image correlation. *J. Strain Anal.*, **43**, 769–780.
37 Roux, S. and Hild, F. (2006) Stress intensity factor measurements from digital image correlation: post processing and integrated approach. *Int. J. Fract.*, **140**, 141–157.
38 Becker, T. H., Mostafavi, M., Tait, R. B. and Marrow, T. J. (2012) An approach to calculate the J-integral by digital image correlation displacement field measurement. *Fatigue Fract. Eng. Mater. Struct.*, **35**, 971–984.
39 Ould, C. B., Imad A. and Benguediab, M. Influence of the cyclic plastic zone size on the propagation of the fatigue crack in case of 12NC6 steel. *Comput. Mater. Sci.*, **43**(2008), 1010–1017.
40 Vic-2D reference Manuel, correlated solution (2009).
41 Mostafavi, M. and Marrow T. J. (2011) *In situ* observation of crack nuclei in poly-granular graphite under ring-on-ring equi-biaxial and flexural loading. *Eng. Fract. Mech.*, **78**(8), 1756–1770.

42 Sutton, M. A., Yan, J. H., Tiwari, V., Schreier, H. W. and Orteu, J. J. (2008) The effect of out-of-plane motion on 2D and 3D digital image correlation measurements. *Opt. Lasers Eng.*, **46**, 746–757.
43 Baccar, M., Shah, M., Velay, V., Mabru, C. and Rézaï-Aria, F. (2012) Analysis of crack propagation and crack tip opening displacements by measurements 2-D digital image correlation in a hot working tool steel. In proceedings of the 9th international tooling conference 2012, leoben.
44 Shah, M., Mabru, C. and Rézaï-Aria, F. (2010) Investigation of crack propagation in X38CrMoV5 (AISI H11) tool steel at elevated temperatures. *Procedia Eng.*, **2**, 2045–2054.
45 El-Shabasy, A. B. and Lewandowski, J. J. (2004) Effects of load ratio, R, and test temperature on fatigue crack growth of fully pearlitic eutectoid steel (fatigue crack growth of pearlitic steel). *Int. J. Fatigue*, **26**, 305–309.
46 Ding, J., Hall, R. and Byrn, J. (2005) Effects of stress ratio and temperature on fatigue crack growth in a Ti-6Al-4V alloy. *Int. J. Fatigue* **27**, 1551–1558.
47 Pelloux, R. M. N. (1969) Mechanisms of formation of ductile fatigue striations. *Trans ASM*, **62**, 281–285.
48 Neumann, P. (1969) Coarse slip model in fatigue. *Acta Metall.*, **17**, 1219–1225.
49 Chow, C. L. and Lu T. J. (1991) Cyclic J-integral in relation to fatigue crack initiation and propagation. *Eng. Fract. Mech.*, **39**(1), 1–20.
50 Ktari, A., Haddar, N., Köster, A. and Marie-Louise Toure, A. (2011) Numerical computation of thermal fatigue crack growth of cast iron. *Fatigue Fract. Eng. Mater. Struct.*, **34**, 498–509.
51 Gasiak, G. and Rozumek, D. (2004). ΔJ-integral range estimation for fatigue crack growth rate description. *Int. J. Fatigue*, **26**, 135–140.
52 Banks-Sills, L. and Volpert, Y. (1991) Application of cyclic J-integral to fatigue crack propagation of Al 2024-T351. *Eng. Fract. Mech.*, **40**(2), 355–370.
53 Chow, C. L. and Lu, T. J. (1989) On the cyclic J-integral applied to fatigue cracking. *Int. J. Fract.*, **40**, 53–59.
54 Hutchinson, J. W. (1968) Plastic stress and strain fields at crack tip. *J. Mech. Phys. Solids*, **16**, 337–342.
55 Tracey, D. M. (1976) Finite element solutions for crack-tip behavior in small-scale yielding. *(American Society of Mechanical Engineers), ASME, Trans., Ser. H-J. Eng. Mater. Technol.*, **98**, 146–151.
56 McMeeking, R. M. (1977) Finite deformation analysis of crack-tip opening in elastic–plastic materials and implications for fracture. *J. Mech. Phys. Solids*, **25**(5), 357–381.
57 McClintock, F. A. (1971) Plasticity aspects of fracture. *Fract. adv. treatise*, **3**, 47–225.
58 Rice, J. and Rosengren, G. F. (1968) Plane strain deformation near a crack tip in a power-law hardening material. *J. Mech. Phys. Solids*, **16**, 1–12.
59 Shah, M. (2010) Investigation of crack propagation in X38CrMoV5 tool steel at room temperature and 600 °C on small scale specimens. PhD thesis, Ecole des Mines d'Albi (France).